Constraining aerosol phase function using dual-view geostationary satellites

Qijing Bian[1], Sonia Kreidenweis[1], J. Christine Chiu[1], Steven D. Miller[2], Xiaoguang Xu[3], Jun Wang[4], Ralph Kahn[5], James A. Limbacher[5,6], Lorraine A. Remer[3], and Robert C. Levy[5]

[1]Department of Atmospheric Science, Colorado State University, Fort Collins, CO, USA
[2]Cooperative Institute for Research in the Atmosphere, Colorado State University, Fort Collins, CO, USA
[3]Joint Center for Earth Systems Technology, University of Maryland, Baltimore County, MD, USA
[4]Department of Chemical and Biochemical Engineering, University of Iowa, Iowa City, IA, USA
[5]NASA Goddard Space Flight Center, Greenbelt, MD, USA
[6]Science Systems and Applications, Inc., Lanham, MD, USA

Corresponding author: Sonia Kreidenweis (soniak@colostate.edu)

Key Points:

- Dual, opposing-view geostationary satellite observations help constrain structural properties of dust scattering phase function
- The newly reconstructed phase function produces consistent aerosol optical depth retrievals between the two satellites
- The retrievals between the two satellites agree within 0.059±0.072, much improved compared to 0.157±0.084 in single view retrievals

Abstract

Passive satellite observations play an important role in monitoring global aerosol properties and helping quantify aerosol radiative forcing in the climate system. The quality of aerosol retrievals from the satellite platform relies on well-calibrated radiance measurements from multiple spectral bands, and the availability of appropriate particle optical models. Inaccurate scattering phase function assumptions can introduce large retrieval errors. High-spatial resolution, dual-view observations from the Advanced Baseline Imagers (ABI) on board the two most recent Geostationary Operational Environmental Satellites (GOES), East and West, provide a unique opportunity to better constrain the aerosol phase function. Using dual GOES reflectance measurements for a dust event in the Gulf of Mexico in 2019, we demonstrate how a first-guess phase function can be reconstructed by considering the variations in observed scattering angle throughout the day. Using the reconstructed phase function, aerosol optical depth retrievals from the two satellites are self-consistent and agree well with surface-based optical depth estimates. We evaluate our methodology and reconstructed phase function against independent retrievals made from low-Earth-orbit multi-angle observations for a different dust event in 2020. Our new aerosol optical depth retrievals have a root-mean-square-difference of 0.028 – 0.087. Furthermore, the retrievals between the two geostationary satellites for this case agree within about 0.06±0.073, as compared to larger discrepancies between the operational GOES products, which do not employ the dual-view technique.

1 Introduction

The advent of high-resolution geostationary satellite observations has revolutionized the monitoring of the temporal evolution of myriad atmospheric and surface phenomena. This capability has led to improved weather forecasts (e.g., Mecikalski et al., 2020), insights into cloud microphysical evolution (e.g., Letu et al., 2019), and better tracking of high-impact events that affect human health, such as smoke plumes and blowing dust (Magnamen et al., 2020; Nichols, 2020; Sorense, et al. 2021). In particular, the two most recent NOAA/NASA Geostationary Operational Environmental Satellites-R series (represented by GOES-East, or GOES-16; and GOES-West, or GOES-17; hereafter, G16 and G17, respectively) provide high quality observations over much of the Western Hemisphere (Figure 1). Among several instruments on board G16 and G17, the Advanced Baseline Imagers (ABI; Schmit et al., 2017) measure reflectances in the visible, near-infrared and thermal infrared spectral regions (0.47 – 13.3 μm) with spatial resolutions of 0.5 – 2 km, offering ~3x higher spectral, ~4x higher spatial, and ~5x higher temporal resolution compared to the previous-generation GOES imagers.

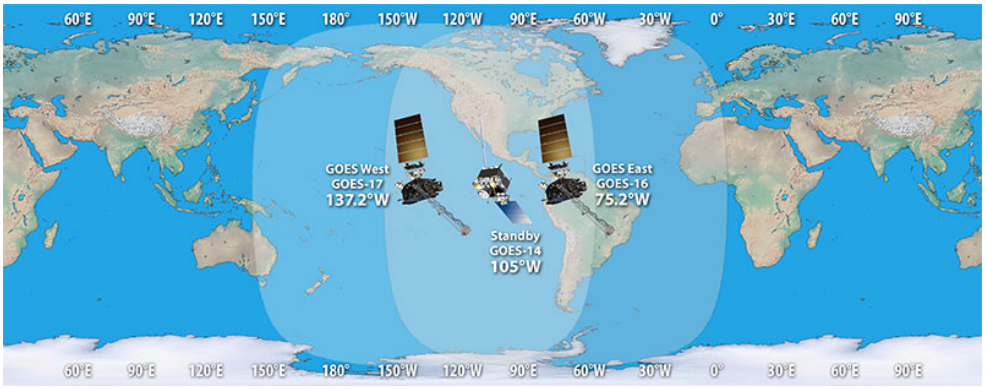

Figure 1. Coverage of GOES-16 and GOES-17. G16 was launched in December 2017 and is located at 75.2° West above the equator; G17 was launched in March 2018 and is located at 137.2° West. This figure is taken from https://www.goes-r.gov/mission/mission.html, credit: NOAA/GOES-R.

Over the past several decades, spaceborne multispectral reflectance measurements in the shortwave region have played a key role in characterizing aerosol properties, as demonstrated both in geostationary (Knapp et al., 2005; Zhang et al., 2013) and polar-orbiting platforms (Miller, 2003; Kahn & Gaitley, 2015; Zhou et al., 2020). Most aerosol optical depth (AOD) retrievals are based on single-view, multi-wavelength reflectances. Under cloud-free conditions, the observed reflectance depends on aerosol optical depth (AOD), single scattering albedo (SSA), the scattering phase function, and properties of the underlying surface reflectance. Therefore, the accuracy of aerosol retrieval hinges on how well these components are constrained by either a priori information or observations. For example, several studies have demonstrated that incorporating information on aerosol SSA and phase functions from NASA Aerosol Robotic Network (AERONET) observations can greatly improve AOD retrievals (Shi et al., 2019; Yang et al., 2019). Likewise, multi-view measurements such as those from the Multi-

angle Imaging SpectroRadiometer (MISR) allow better constraints on aerosol model selections (Si et al., 2021) by sampling a portion of the phase function.

As seen in Figure 1, the G16 and G17 ABI fields of view offer considerable overlap over the conterminous United States and the Eastern Pacific Ocean. The dual-viewing geometry available in this broad zone allows for additional constraint on phase function (Chylek et. al., 2003; the ABI Algorithm Theoretical Basis Document (ATBD), 2018) in ways analogous to MISR retrievals. To understand the potential usefulness of the dual views, Figure 2 highlights the pairs of scattering angles simultaneously observed from G16 and G17 in all seasons for several locations in North America. The corresponding scattering angle combinations largely fall within the range between 90° and 180°, indicating that the dual views would be particularly useful if aerosol phase function features in this scattering range are a focus.

Scattering angles between 90° and 180° are critical for distinguishing between spherical and non-spherical particles (e.g., Kahn et al., 1997). The former are generally consistent with properties of non-absorbing marine and pollution aerosols, whereas the latter are generally consistent with dust particles that have irregular shapes. Although highly scattering spherical particles have a distinct backward scattering peak, non-spherical particles have a relatively smooth phase function structure in the backscattering hemisphere. Despite significant advances in terms of modeling of irregular particles (Saito et al., 2021), *a priori* selection of the most appropriate dust phase function is not straightforward due to the large variability in and the large number of possible combinations of particle size distribution, shape, aspect ratio, and orientation in the atmosphere (Dubovik et al., 2006; Wang et al., 2020).

Because uncertainties in phase function lead to the largest errors in AOD retrieved at large (i.e., backscatter) scattering angles, Chylek et al. (2003) suggests circumventing these uncertainties by engineering orbits and viewing geometries such that retrievals are based on moderate scattering angles (50 ~ 100˚) at which spherical and nonspherical phase function differences are minimal. However, such an orbit design is impractical to achieve large spatial converge (which often requires nadir view). In contrast, with GOES-8 data, Wang et al. (2003a) demonstrate that the backscatter of the same aerosol plume, as viewed from multiple backscattering angles (>110˚) in several hours by a geostationary satellite, can provide strong constraint on the aerosol phase function. Here, with more recent and advanced GOES satellites, we propose a new and alternative approach that capitalizes on the differences in *simultaneous* measurements at more than one scattering angle >90° to distinguish between non-absorbing spherical and nonspherical particles. As seen in Figure 2, the G16 and G17 observational pair covers a broad range of scattering angles, most of which are larger than 110˚. Therefore, dual-angle retrievals from both G16 and G17 as well as the single-view retrievals from either G16 or G17 will enable large spatial converge of AOD retrieval while maintaining a simultaneous ability to characterize aerosol phase function.

In this work, we explore a method for leveraging the synergy between G16 and G17 geostationary satellite observations, including the pairs of angles that view the same scene, to determine a best-fit aerosol scattering phase function. Specifically, we propose a method for adjusting an initial guess of a mineral dust phase function to obtain consistent AOD retrievals

across the observed scattering angles for a selected case study of a Saharan dust plume which was transported over the Atlantic Ocean and reached the Gulf of Mexico. We test the applicability of the resulting adjusted phase function by retrieving AOD from G16 and G17 reflectances for an additional case of long-range-transported Saharan dust and compare our retrievals with those from the MISR and the operational GOES aerosol products.

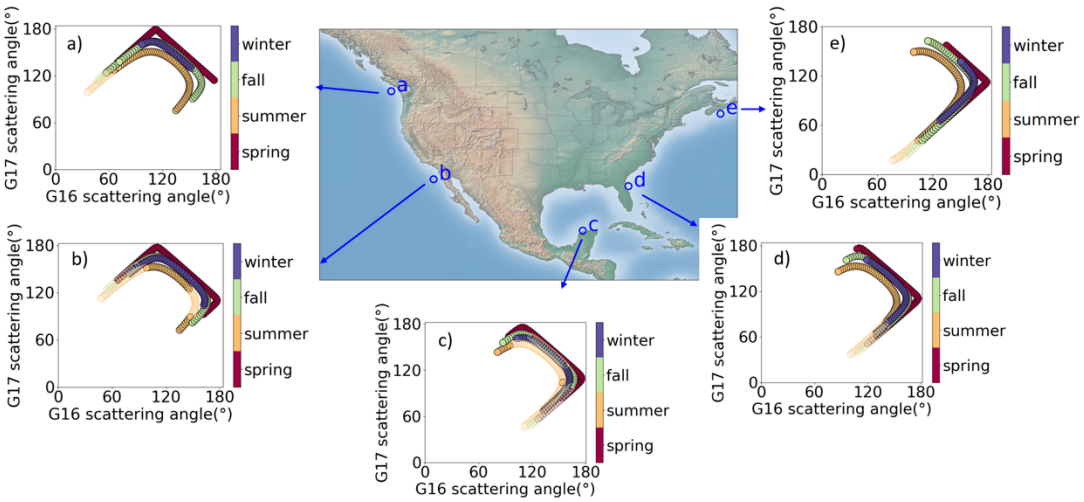

Figure 2. Scattering angle pairs of G16 and G17 for selected locations, including (a) (48°N, 126°W), (b) (31°N 118°W), (c) (21°N, 90°W), (d) (30°N, 81°W) and (e) (44°N, 63°W). Calculations were performed over the course of sunrise to sunset on 1st of March, June, September, and December to represent different seasons. Defining a sun glint region where the glint angle is less than 40°, color-filled symbols represent that the pixels are outside the sun glint region and can be used in the proposed methodology. In contrast, unfilled symbols represent pixels that are within the sun glint region and will be excluded for retrieval.

2 Methods

2.1 Dust case study

The Gulf of Mexico is frequently impacted by long-range transported Saharan dust during the summer season from June to September (Carlson and Prospero, 1972; Prospero and Lamb, 2003). As shown in Figures 1 and 2c, this location resides in the overlap region of G16 and G17, with simultaneous observations available from two view angles. We selected a Saharan dust plume event, which was observed and forecasted (e.g., by the Navy Aerosol Analysis and Prediction System, https://www.nrlmry.navy.mil/aerosol/; Westphal et al., 2009) in its traverse across the Atlantic Ocean. This plume arrived in the Gulf of Mexico around 23 June 2019. We restricted our study of this case to an over-ocean region to minimize uncertainties associated with land surface reflectance (e.g., Zhang et al., 2020). During this period, fires were observed on the Yucatán peninsula and elsewhere in the region, so that some smoke was likely present in addition to sea salt and dust aerosols. However, the case is dust-dominated, as evidenced by the information to follow.

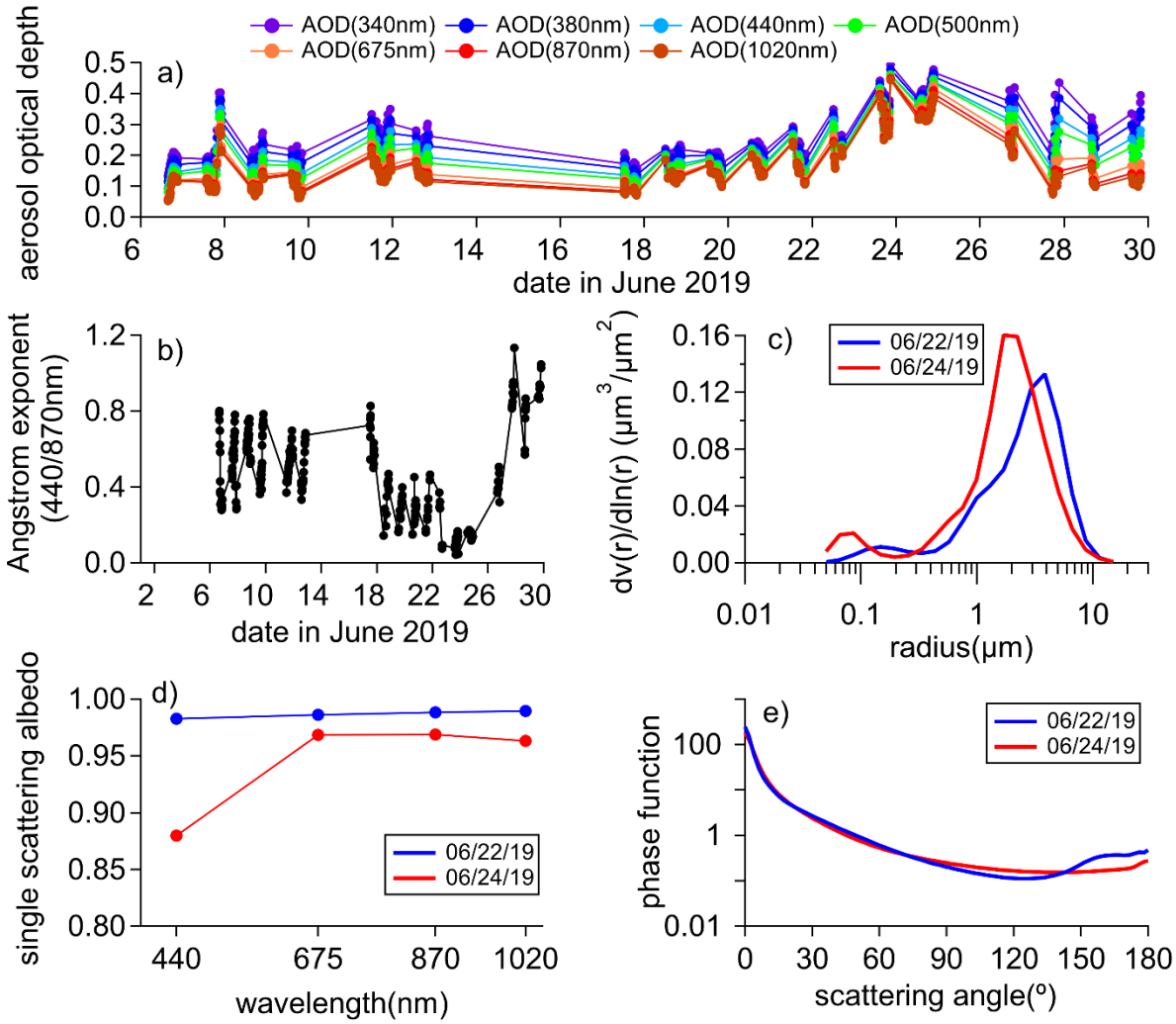

Figure 3. AERONET Level l.5 retrieval products at the Merida site (Level 2 data were unavailable for this case), used for reconstructing the dust phase function. (a) AOD and (b) Angström exponent during June 2019. (c), (d) and (e) provide averaged volume particle size distributions, single scattering albedos, and phase functions (at 675 nm), respectively, specifically for 22 and 24 June 2019. The AERONET observations are described further in Appendix A.

Data from this Saharan dust-dominated case study are shown in Figure. 3. This dust event was clearly seen in the AERONET observations at the Merida site (20.984°N, 89.645°W) on the Yucatán Peninsula, as indicated by the peak in AOD and the weak spectral dependence of AOD (a characteristic of large particles relative to the wavelength of light) (Figure 3a). The only day during the elevated AOD period with reported AERONET particle property retrievals was 24 June. The presence of dust on 24 June was indicated by the small value of the Angstrom parameter (Figure 3b) and the retrieved volume size distribution of particles in Figure 3c, which was dominated by the coarse mode. The wavelength dependence of the retrieved single

scattering albedo (SSA; Figure 3d) was also similar to that described by Li et al. (2015) for dust. As expected, the retrieved phase functions were flat in the scattering angle range between 100 and 160° (Figure 3e), distinguishing these aerosols from spherical particles. In contrast, although the data on 22 June also indicated a coarse-mode-dominated aerosol, the lower AOD, higher SSA, and spherical-like phase function suggested the likely dominance of sea salt.

As shown in Figure 4, the AERONET AOD at Merida was fairly constant throughout the day on 24 June 2019. For comparison, G16 and G17 operational (i.e., single-view, stand-alone) AOD retrievals for a coincident oceanic pixel in the Gulf of Mexico near Merida (within ~50 km) are also shown. Their agreement with AERONET is reasonable for part of the day. However, during the periods of temporal overlap, the G16 and G17 AODs are not in agreement with each other, indicative of errors in the surface model, aerosol model, or both. We note that for the latitude, longitude, and date of this case study (Fig. 2c), the periods of overlap when both sensors were outside of sun glint were minimal: there was one overlapping time stamp at 16:40 UTC, and a series of nine overlapping points after about 22:00 UTC. Thus, we used comparisons against AERONET and head-to-head comparisons in the post-22:00 UTC time frame when validating this new retrieval scheme.

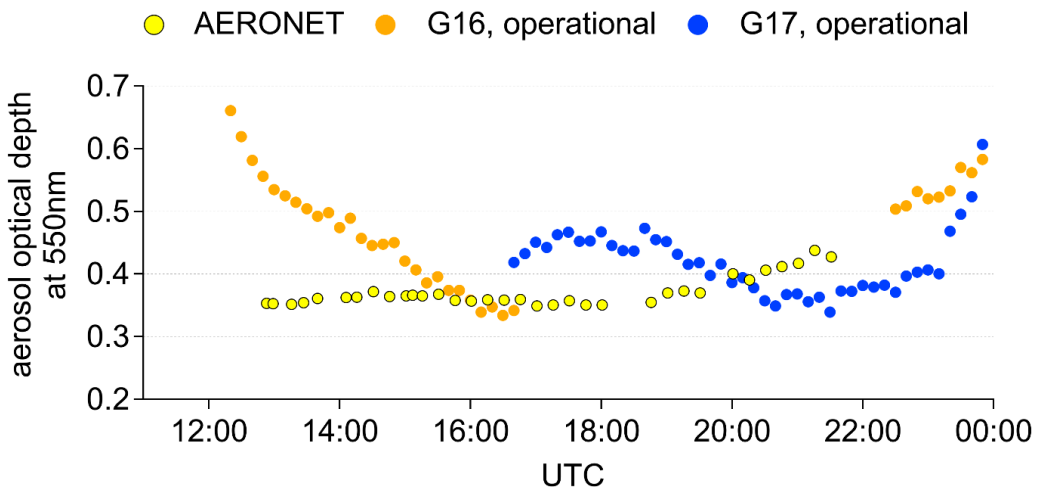

Figure 4. AERONET-derived aerosol optical depths at 550 nm on 24 June 2019 at the Merida site (20.984°N, 89.645°W), along with G16 and G17 operational products for a pixel located at (21.452°N, 89.604°W). The GOES operational products are described further in Appendix B.

2.2 Retrieval method

In GOES Mode 6 operations, the ABI provides full disk images every 10 min and measures radiance in 16 spectral bands. In this study, we used full disk imagery reflectances at the 640 nm wavelength (ABI Band 02; 500 m resolution at nadir) and retrieved AOD over ocean pixels. To retrieve AOD from ABI reflectances, we used a look-up table (LUT) approach, based on calculations from the Unified Linearized Vector Radiative Transfer Model (UNL-VRTM, Xu

and Wang, 2019) with VLIDORT (Spurr et al., 2006) as the core radiative transfer code. The UNL-VRTM has the capability for line-by-line gas absorption calculations from the HITRAN database, including its ancillary UV-visible cross-sections for water vapor continuum absorption and Chappuis ozone absorption. It also includes Rayleigh, Mie and T-matrix scattering codes (Wang et al., 2014). The model has been validated in and used by several remote sensing theory studies (Xu and Wang, 2015; Ding et al., 2016) and aerosol retrieval algorithms for surface (Xu et al., 2015), airborne (Hou et al., 2020) and spaceborne instruments (Xu et al., 2017, 2019).

The UNL-VRTM requires aerosol SSA, phase function, optical depth, layer height and geometric thickness, and ocean surface reflectance to simulate ABI reflectances. The aerosol was represented using the 24 June 2019 AERONET-derived optical properties as a first guess: SSA was therefore set equal to 0.975 (per Fig. 3d) and the averaged the phase function shown in Fig. 3e was input as discrete points with the same scattering angle resolution as the AERONET product. The LUT was constructed for a uniform aerosol layer at 2–4 km with optical depths varying from 0 to 3. Note that at the atmospheric window, the AOD retrieval is not sensitive to vertical distribution of aerosols (Wang et al., 2003b). The bi-directional ocean reflectance was calculated using the method of Cox and Munk (1954), requiring information on ocean surface wind speed. We input the time-varying wind speed available in the NCEP North American Regional Reanalysis data, which was 7–11 m s^{-1} for this case. To account for water-leaving radiance, a Lambertian albedo of 0.0009–0.0035, calculated offline from the subroutine in the Spherical Harmonics Discrete Ordinate Method package (SHDOM, Evans, 1998), was added to the final ocean reflectance distribution.

Under these first-guess assumptions, Figure 5a shows the retrieved AOD from G16 and G17 reflectance observations at 640 nm with an on-ground spatial resolution of 500 m. For comparison, AERONET AOD values are co-plotted, using the Angstrom exponent to interpolate to 640 nm. Although the time-dependence of retrieved AOD is more similar to that of AERONET as compared with the GOES operational products shown in Figure 4, both G16 and G17 retrieved AODs are systematically biased high compared to AERONET. Further, as is seen with the GOES operational products, the AODs do not match in the overlap regions, with 4–20% differences. In this 12-h period, Figure 5b shows that most of the observations occurred for scattering angles > 105˚, the backscatter region noted by Chylek et al. (2003) to be most sensitive to uncertainties in the assumed aerosol model. Following Chylek et al. (2003), we hypothesize that errors in the phase function are more significant than surface reflectance, and seek to improve the retrievals by adjusting the phase function, with a particular focus on the angles at which the mismatch is greatest. As shown in Figure 5c, the differences between the retrieved AODs and the AERONET observations are large for scattering angles between ~110° and 150°, suggesting that changes to the phase function are needed over this range. The methodology for doing so is described in the next section.

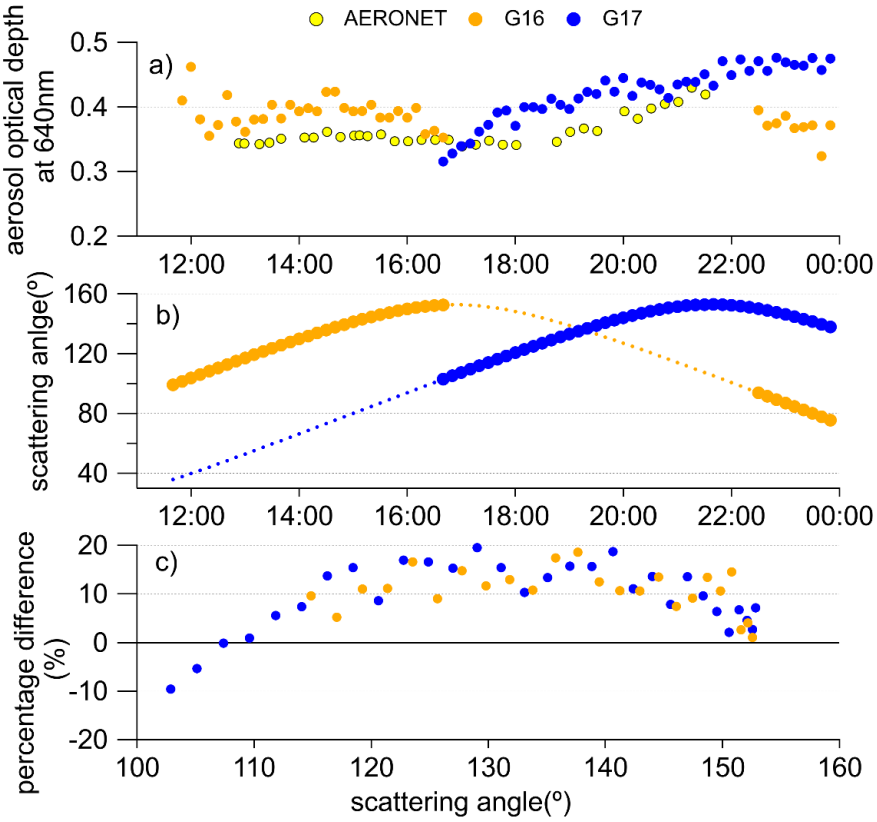

Figure 5. (a) AOD retrievals at 640 nm from the AERONET Merida site, and from G16 and G17 observations using the SSA and phase function from the 24 June 2019 AERONET inversions at Merida. (b) The corresponding scattering angles for G16 and G17 over the course of the case study day. The dotted lines represent data points for which the glint angle is < 40°. (c) AOD percentage difference (((retrieved AOD – obs. AOD)/obs. AOD) × 100%) as a function of the scattering angle, where obs. AOD is from AERONET. AERONET AODs were interpolated to the G16 and G17 time stamps for this comparison.

2.3 Adjusting the phase function

The ABI-observed reflectance is proportional to the product of ambient AOD, SSA and phase function. Therefore, to reduce the differences shown in Figure 5c, we tested the impact on the retrievals of phase functions that had been adjusted between scattering angles of ~110°–150° by 20%, 30% and 35%, respectively. The modified phase functions were smoothed using a moving average with five neighboring values before they were input to the radiative transfer model. SSA was held constant at the original value (0.975) for these tests.

Our results show that the phase function adjusted by 30% (Figure 6) resulted in AOD retrievals that best fit the AERONET observations (±10%, Figure 7). Further, the average percentage difference between G16 and G17 during the overlapping period after 22:00 UTC was reduced to 4%. As equivalency of G16 and G17 retrieved AODs during periods of overlap is a

requirement for a valid retrieval, this improved agreement further supports that the adjusted phase function is more appropriate to the selected case study.

The adjusted phase function has enhanced side scattering. We note the similarity, over the common range of angles, to the phase function computed for a population of spheroid dust particles with aspect ratio of 1.8. This phase function was constructed using the database described in Meng et al. (2010) along with the AERONET-derived size distribution and SSA for our case (Figure 3). Laboratory measurements (e.g., Muñoz et al., 2001; Volten et al., 2001) suggest that the dust phase function tends to be flat and featureless, but it has not been demonstrated that this is the best choice for satellite-based retrievals. Extending this adjustment approach to various locations and transport events will help reduce the uncertainty in the dust phase function, and may suggest its relationship to the microphysical evolution of aerosol particles.

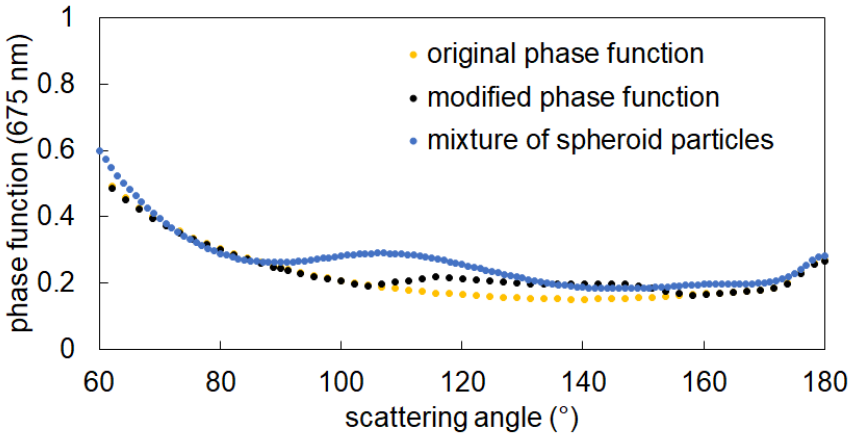

Figure 6. Comparison of original AERONET phase function (golden dots) and modified phase function (black dots) after increasing the original phase function by 30%. This adjustment was based on the differences between observed and retrieved AODs at scattering angles of 110°–150°. The adjusted phase function is smoothed and normalized. For context, a phase function from a mixture of spheroid dust particles (Meng et al., 2010) is co-plotted with blue dots.

3 Comparisons to other independent retrievals

To test whether the adjusted phase function is applicable to other dust cases observed by G16 and G17, we selected an additional case study from June 2020. The period of interest occurred during a large and extended (mid through late June) Saharan dust transport event that affected the Gulf of Mexico and a large portion of the southeastern United States (Francis et al., 2020). We conducted retrievals using our methodology and compared them against AODs retrieved from the MISR standard and research algorithms. In principle, an ideal case would be associated with the highest AODs observed in the Gulf of Mexico within the main dust plume during 23–27 June 2020. Unfortunately, after excluding cloudy and glint regions and attempting to maximize the overlap time between G16 and G17 retrievals over the MISR swaths, the best case was on 29 June 2020, past the date of major plume event.

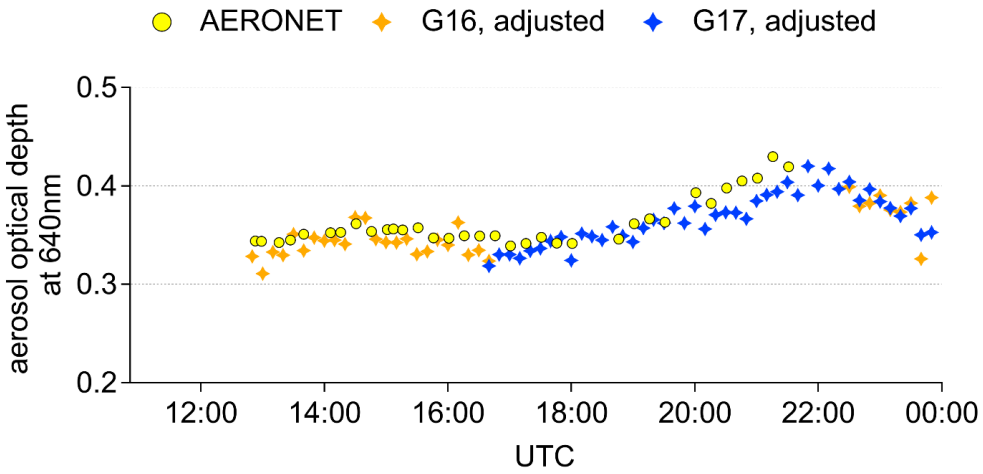

Figure 7. Same as Figure 5a, but using the adjusted phase function shown in Figure 6 to re-build the look-up tables for the G16 and G17 retrievals.

For 29 June 2020, retrievals from the MISR research algorithm (Limbacher & Kahn, 2019) in Figure 8, performed at 1.1 km pixel resolution, shows that the dominant aerosol type over the ocean north and northwest of the Yucatán peninsula was indeed dust-like, with AODs between ~0.4–0.6 (Figure 8a). The mid-visible AOD fraction of non-spherical dust particles was about 0.6 and the fine mode fraction was generally less than 0.4. The single scattering albedo was also consistent with the value found in the previous case study. These results confirm the dominance of dust aerosol even though the major plume had already passed. Note that the region just north of the Yucatán peninsula was affected by considerable thin cirrus and is very close to the solar equator. Both these conditions affect the quality of the MISR retrievals. In particular, the range of scattering angles observed by MISR is diminished when the sun is high in the sky, which directly affects particle-type discrimination. Therefore, the MISR Research Algorithm used a limited particle climatology to reduce retrieval noise, comprised of six component optical models: three spherical models in common with the MISR standard algorithm, two additional spherical models, and a non-spherical dust optical analog.

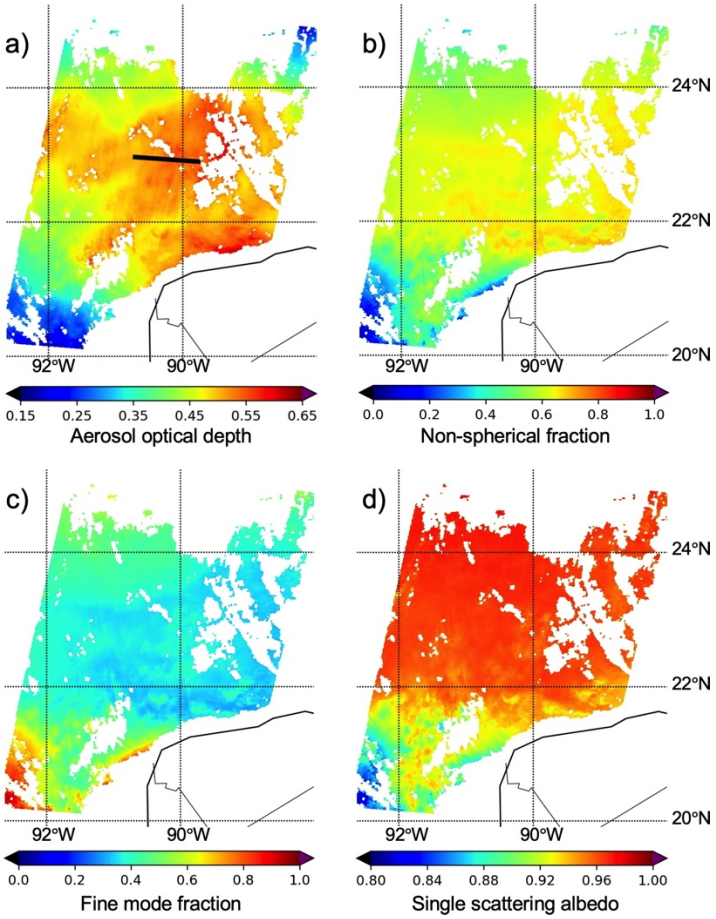

Figure 8. Map of retrieved (a) aerosol optical depth, (b) non-spherical AOD fraction, (c) fine mode fraction, and (d) single scattering albedo at about 17:00 UTC on 29 June 2020, as determined by MISR Research Algorithm retrievals for Orbit 109209. Cloud contamination precludes retrievals (white areas) over most of the land (southeast corner) as well as the northern and much of the eastern parts of the scene. In the southwest corner, retrieved particles are smaller, darker, and mostly spherical, likely smoke from the Yucatan. The line in (a) indicates the pixels selected for further intercomparisons. The MISR retrieval products are described further in Appendix B.

Figure 9 shows detailed retrievals for selected pixels that were considered cloud-free and away from glint regions. All points represent the mean AODs aggregated from pixels within 2.4 km regions, and the error bars represent the standard deviation of the retrieval results. In general, the AOD from the MISR Research Algorithm was systematically ~0.015–0.02 higher than the standard algorithm, well within the uncertainty range of the retrievals and likely attributable to differences in the dust optical model used.

Examining Fig. 9, compared to retrievals from the MISR Research Algorithm the operational G16 retrieved AODs were smaller by 0.061±0.032 and the operational G17 AODs were larger by 0.158±0.022. Errors reported here represent the mean absolute bias ± standard

deviation. In addition, the differences between G16 and G17 in the operational retrievals were large, indicating errors in the selected aerosol model. Among G16 and G17 retrievals, the retrieval from G17 observations using our adjusted phase function shows the best agreement with MISR, with errors of 0.015 ± 0.012, and most points fall within one standard deviation of the aggregated MISR retrievals. Our new G16 retrievals are the second closest ones, with errors of 0.034± 0.023. The G16 and G17 retrievals using our adjusted phase function agreed only within 0.043±0.016, suggesting that the aerosol model was not fully optimized despite improvement over the operational retrieval. However, we cannot rule out that possible calibration differences between the two instruments can contribute to this offset, along with errors on modeling ocean surface reflectance.

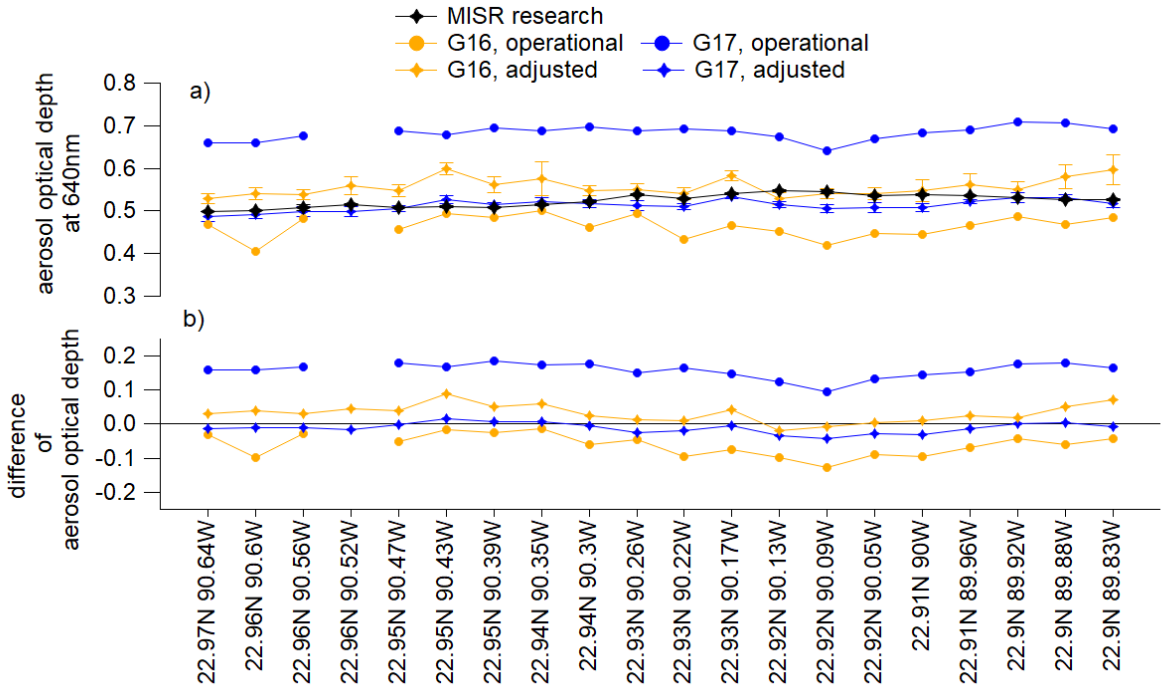

Figure 9. Retrieved AODs at 640 nm for selected pixels that are marked by a line in Figure 8a. Retrievals include those from the MISR Research Algorithm, the GOES operational products, and GOES using our adjusted dust phase function. All products except the ones using the adjusted phase function report AODs at 550 nm and have been converted to 640 nm using spectral scaling coefficients available in the standard MISR product. (b) AOD difference compared to those from the MISR Research Algorithm.

Although MISR retrievals have the advantage of multi-angle views that are helpful for evaluating the angular dependencies in the GOES retrievals, the MISR overpass time of 17:00 UTC poses challenges. At 17:00 UTC, the corresponding angles over the Gulf of Mexico for G16 and G17 are 152° and 107°, respectively. Recall per Fig. 6 that these angles are close to the

boundaries of the adjusted portion of the phase function. Therefore, we extended G16 and G17 retrievals to the entire daytime period, evaluating the success of these retrievals by the consistency between G16 and G17 retrievals during periods of overlap.

Taking retrievals from the 6th and 12th pixel from Figure 9 as examples, Figure 10 shows that the operational G16 and G17 retrievals have very similar patterns – starting with a larger AOD at scattering angle of ~107° and then decreasing and ending with a smaller AOD at scattering angle of ~150°. This is a signature of the influence of spherical phase functions, which is not surprising because the operational GOES algorithm employs only spherical aerosol models. The AOD differences between G16 and G17 operational retrievals in the overlap period for all 20 pixel-locations have a mean of 0.157 and standard deviation of 0.084. In contrast, as shown in Figure 10, G16 and G17 retrievals using the adjusted phase function agreed well in the overlap period, with AOD differences of 0.059±0.072 for all 20 pixel-locations (See Appendix C for further details). The improved agreement between the two AODs suggests that the adjusted phase function is more appropriate.

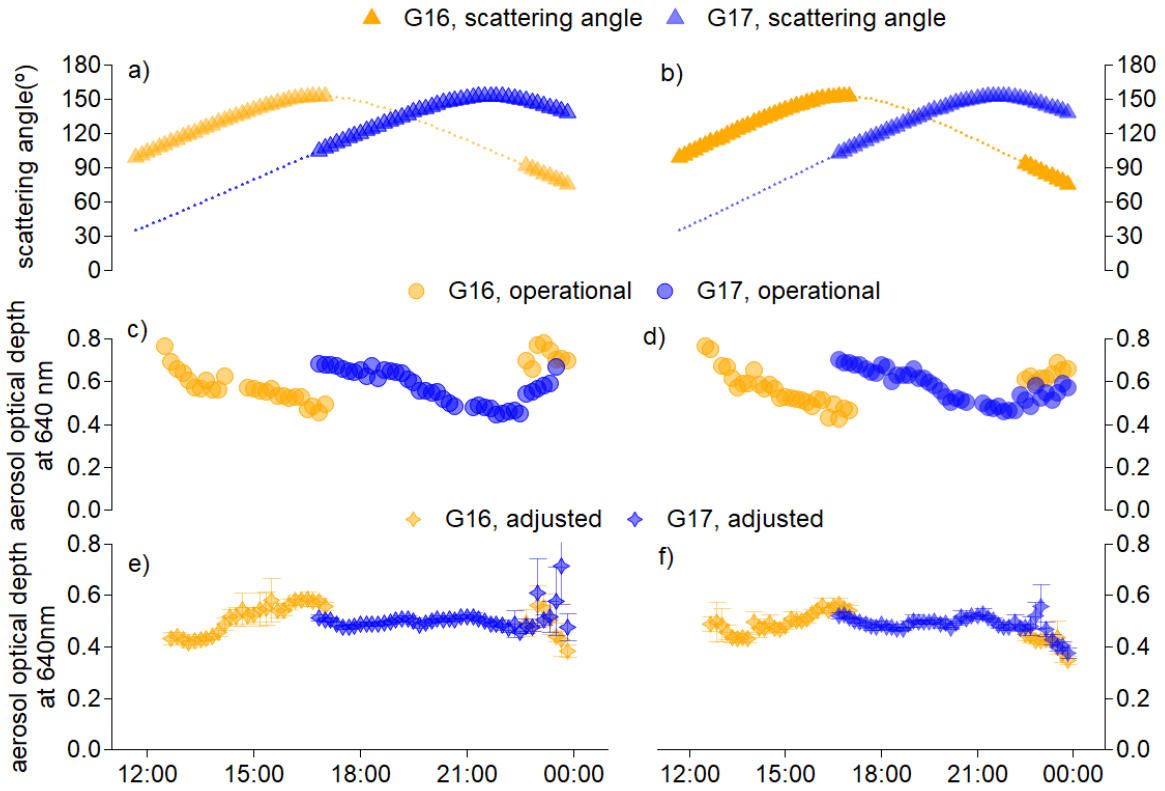

Figure 10. Scattering angle (a) and retrieved aerosol optical depths at 640 nm (c) from the operational GOES products and (e) those using the adjusted phase function for the 6th pixel shown in Figure 9. (b), (d) and (f) on the right panel are same as (a), (c) and (e), respectively, but for the 12th pixel.

4 Summary

In this study, we explored the use of overlapping ABI observations from GOES-16 and GOES-17 to constrain aerosol retrievals, as well as exploiting observations at specific scattering angles to adjust the shape of an *a priori* phase function used to create look-up tables. The complex nature of mineral dust particles confounds attempts to determine the most appropriate phase functions from first principles. This difficulty motivated our attempt to use observations directly to deduce a best-fit dust phase function, taking advantage of the ranges of scattering angles represented in the data from the two satellites.

We found that the revised phase function based on the dual-view technique led to better agreement between the G16 and G17 retrievals, compared with the operational products, supporting the validity of the results. Co-locating with AERONET or another measure of AOD was important, as the methodology requires separate, accurate measurements of the AOD to serve as one of the constraints. Further exploration of this approach can therefore be undertaken by conducting retrievals over AERONET sites that encompass the range of paired observations shown in Figure 2, also covering a range of aerosol types across the varied locations. The approach may be especially useful for smoke, for which differences in optical properties have been shown between fresh and aged emissions, and the findings used to recommend optimized fresh and aged smoke phase functions.

The representation of the angular scattering from the surface is an important consideration in applying this methodology, as it relies so critically on using the variability across scattering angles to evaluate the applied phase function. Over land, as discussed by Zhang et al. (2020), limitations in the representations of land surface reflectances lead to biases in retrievals for geostationary observations. The surface models used in retrievals for polar-orbiting satellite observations have not been optimized for the different geometries accessed by the geostationary instruments. Over-land retrievals present a more challenging situation for our proposed methodology, as both the surface reflectances and the aerosol model may require adjustment. The use of overlapping G16 and G17 observations provides an additional, helpful constraint for such cases.

Appendix A: Ground-based observations

AERONET is a ground-based worldwide network that has routinely monitored aerosol microphysical and optical properties for more than 25 years (Holben et al., 1998). AERONET is composed of sun/sky radiometers that measure radiance in the visible and near-infrared spectral regions with a 1.2° field-of-view. Direct Sun measurements are used to retrieve aerosol optical depth, whereas sky radiance measurements are used to retrieve index of refraction, aerosol size distribution, phase function, and single scattering albedo. As Level 2 products were not available for the sites of interest in this study, we used V3 Level 1.5 products, which are quality controlled through automatic cloud screens but have not had post-field calibrations applied to the retrievals. Although the exact bias and uncertainty in Level 1.5 data are instrument dependent, the

differences in AOD between these two levels has a mean of 0.02 and one standard deviation of 0.02 (Giles et al., 2019).

The dust model used in the AERONET retrieval method is detailed in Dubovik et al. (2006). To account for the nonsphericity of dust, they consider mixtures of randomly oriented spheroids with various shapes from flattened to elongated spheroids. By incorporating these mixtures, the resulting phase function was in better agreement with laboratory observations and smoother at scattering angles between 100° and 160° than prior estimates that considered a single fixed axis ratio distribution.

Appendix B: Satellite datasets for evaluation

For pixels over ocean, the GOES operational aerosol retrieval algorithm (the ABI Algorithm Theoretical Basis Document, 2018) used four fine modes and five coarse modes, the same as used in MODIS Collection 5 products (Remer et al., 2005, 2006; Levy et al., 2007). Aerosol retrievals were performed by matching the observed reflectance at 640, 864, 1610 and 2240 nm wavelengths with the pre-calculated lookup tables, based on the methods described in Tanré et al. (1997) and Vermote et al. (2006). The AOD retrieval is available at a temporal resolution of 10 min and a spatial resolution of 2 km at nadir. The uncertainty in retrieved AOD over the ocean is reported as 0.03±0.05AOD.

In addition to the operational ABI aerosol product, we compared our retrievals to those from MISR. MISR on the NASA Terra satellite measures reflectances from nine different angles, in each of four spectral bands across the visible and near-infrared (Diner et al., 1998). MISR has a ~380 km swath and a pixel resolution ranging from 275 m near-nadir to 1.1 km off-nadir. The MISR research algorithm is constructed to optimize particle-type discrimination with 1.1 km pixel-level retrievals and is run on a case-by-case basis (Limbacher & Kahn, 2019). The algorithm includes options to self-consistently retrieve the surface and aerosol, or to prescribe the surface from external sources. Retrievals are performed at 1.1 km pixel resolution. Where retrieval conditions are ideal, the algorithm minimizes the cost function using17 component optical models in the algorithm lookup table. For the dust case analyzed in the current study, the scene was largely cirrus-contaminated and the range of scattering angles was small due to high sun elevation angle, a more limited set of component optical models was used for the retrievals shown in Figures 8 and 9.

Appendix C: Retrievals for the remaining 18 pixels

Retrievals for the remaining 18 pixels in Figure 9 are shown in Figure 11. Similar to the example given in Figure 10, the AOD differences between G16 and G17 operational retrievals in the overlap period are generally larger than those between G16 and G17 retrievals using the adjusted phase function. This evaluation indicates that the improved agreement between the G16 and G17AODs is robust.

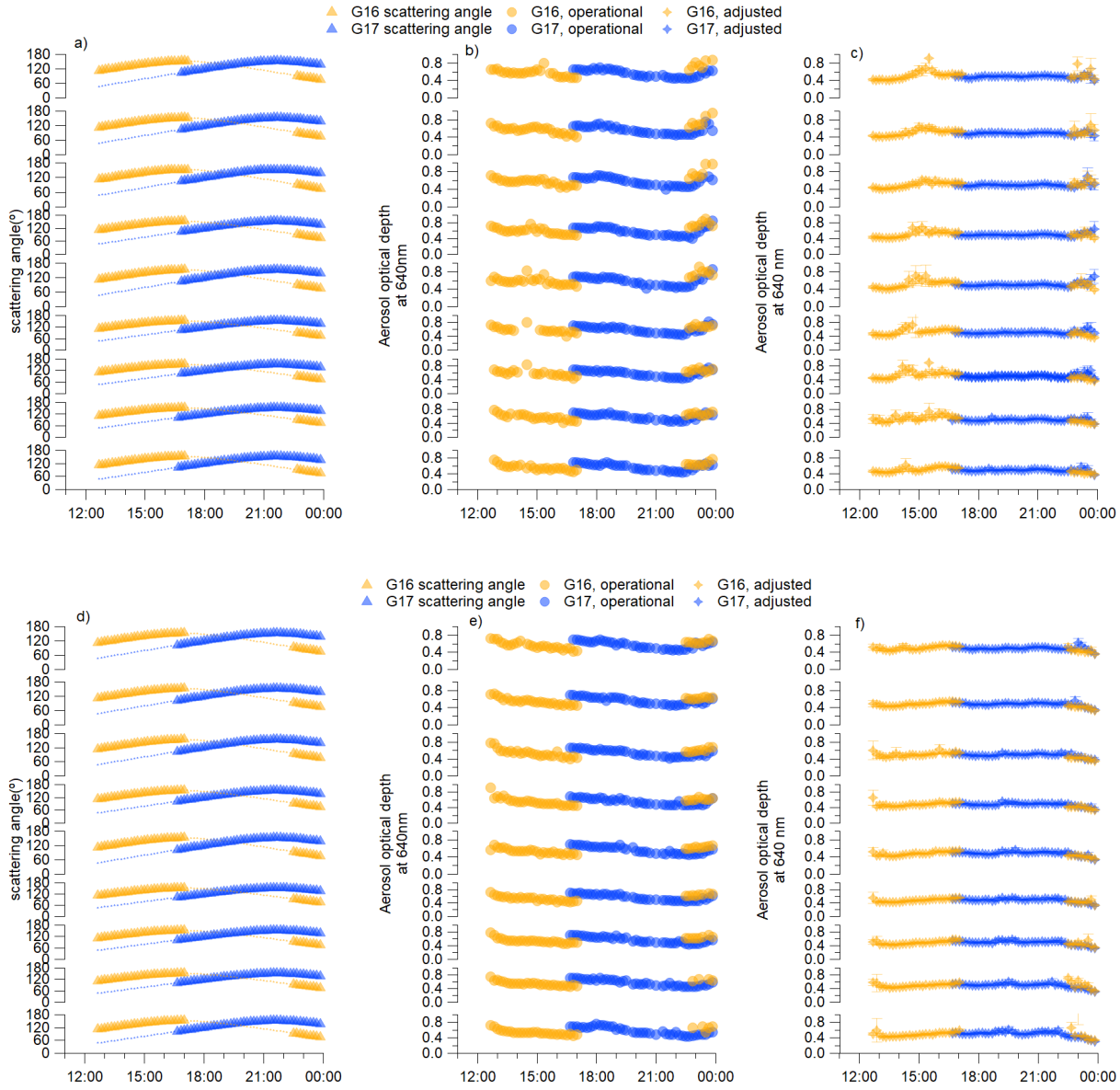

Figure 11. Plots of a) scattering angles, and retrieved aerosol optical depths from (b) GOES operational products, and from c) GOES observations but using the adjusted phase function, for the first 10 pixels in Figure 9 (with the 6th pixel excluded). (d)–(f) are same as (a)–(c), but for the last 10 pixels in Figure 9 (with the 12th pixel excluded).

Acknowledgments, Samples, and Data

This work is based upon research supported by the U. S. Office of Naval Research under Multidisciplinary University Research Initiative (MURI) Grant N00014-16-1-2040. JW and XX are supported by the same MURI grant to the University of Iowa. RK and JAL are supported by

NASA's Climate and Radiation Research and Analysis Program under Hal Maring, the Atmospheric Composition Program under Richard Eckman, and the EOS Terra and MISR projects. NASA's Making Earth System Data Records for Use in Research Environments (MEaSUREs) program (NNH17ZDA001N-MEASURES) provided partial support of LR and RL. All the retrievals presented in the paper will be made freely available through the Mountain Scholar data repository. We thank Hector R. Estevez, Instituto de Geofísica, Universidad Nacional Autónoma de México, for his effort in establishing and maintaining the Mérida site. AERONET data and products can be freely accessed via https://aeronet.gsfc.nasa.gov/new_web/. The operational GOES aerosol products for both satellites were available as of 1 January 2019, at *https://www.avl.class.noaa.gov/saa/products/search?sub_id=0&datatype_family=GRABIPRD&submit.x=28&submit.y=2*.

References

ABI AOD ATBD: GOES-R Advanced Baseline Imager (ABI) algorithm theoretical basis document for suspended matter/aerosol optical depth and aerosol size parameter, NOAA/NESDIS/STAR, Version 4.2, 14 February 2018, available at: https://www.star.nesdis.noaa.gov/smcd/spb/ aq/AerosolWatch/docs/GOES-R_ABI_AOD_ATBD_V4.2_ 20180214.pdf (last access: 24 February 2020), 2018.

Carlson, T. N., & Prospero, J. M. (1972). The large-scale movement of Saharan air outbreaks over the Northern Equatorial Atlantic. *J. Appl. Meteorol*., *11*, 283–297.

Chylek, P., Henderson, B. G., & Mishchenko, M. (2003). Aerosol radiative forcing and the accuracy of satellite aerosol optical depth retrieval. *J. Geophys. Res*., 108(D24), 4764, doi:10.1029/2003JD004044

Chylek, P., Henderson, B. G., & Lesins, G. (2005). Aerosol optical depth retrieval over the NASA Stennis Space Center: MTI, MODIS, and AERONET. *IEEE Transactions on Geoscience and Remote Sensing*, 43(9), 1978–1983. doi: 10.1109/TGRS.2005.851773

Cox, C. & Munk, W. H. (1954), The measurement of the roughness of the sea surface from photographs of the sun glitter. *J. Opt. Soc. Amer*., *44*, 838–850.

Diner, D. J., Beckert, J. C., Reilly, T. H., Bruegge, C. J., Conel, J. E., Kahn, R. A., Martonchik, J. V., Ackerman, T. P., Davies, R., Gerstl, S. A. W., Gordon, H. R., Muller, J. P., Myneni, R. B., Sellers, P. J., Pinty, B., & Verstraete, M. M. (1998). Multiangle Image Spectroradiometer (MISR) instrument description and experiment overview. *IEEE T. Geosci. Remote Sens*., *36*, 1072–1087.

Ding, S., Wang, J., & Xu, X. (2016). Polarimetric remote sensing in O2 A and B bands: Sensitivity study and information content analysis for vertical profile of aerosols. *Atmospheric Measurement Techniques*, *9*, 2077–2092, doi:10.5194/amt-9-2077-2016

Dubovik, O., et al. (2006). Application of spheroid models to account for aerosol particle nonsphericity in remote sensing of desert dust. *J. Geophys. Res*., *111*, D11208, doi:10.1029/2005JD006619

Evans, K. F. (1998). The spherical harmonics discrete ordinate method for three-dimensional atmospheric radiative transfer. *J. Atmos. Sci*., *55*, 429–446, doi:10.1175/1520-0469(1998)055<0429:Tshdom>2.0.Co;2

Francis, D., Fonseca, R., Nelli, N., Cuesta, J., Weston, M., Evan, A., & Temimi, M. (2020). The atmospheric drivers of the major Saharan dust storm in June 2020. *Geophysical Research Letters*, *47*, e2020GL090102. https://doi. org/10.1029/2020GL090102

Garay, M. J., Witek, M. L., Kahn, R. A., Seidel, F. C., Limbacher, J. A., Bull, M. A., Diner, D. J., Hansen, E. G., Kalashnikova, O. V., Lee, H., Nastan, A. M., & Yu, Y. (2020). Introducing the 4.4 km spatial resolution Multi-Angle Imaging SpectroRadiometer (MISR) aerosol product. *Atmos. Meas. Tech*., *13*, 593–628, https://doi.org/10.5194/amt-13-593-2020

Giles, D. M., Sinyuk, A., Sorokin, M. G., Schafer, J. S., Smirnov, A., Slutsker, I., Eck, T. F., Holben, B. N., Lewis, J. R., Campbell, J. R., Welton, E. J., Korkin, S. V., & Lyapustin, A. I. (2019). Advancements in the Aerosol Robotic Network (AERONET) Version 3 database – automated near-real-time quality control algorithm with improved cloud screening for Sun photometer aerosol optical depth (AOD) measurements. *Atmos. Meas. Tech*., *12*, 169–209, https://doi.org/10.5194/amt-12-169-2019.

Holben, B. N., Eck, T. F., Slutsker, I., Tanré, D., Buis, J. P., Setzer, A., Vermote, E., Reagan, J. A., Kaufman, Y. J., Nakajima, T., Lavenu, F., Jankowiak, I., & Smirnov, A. (1998). AERONET – Federated instrument network and data archive for aerosol characterization. *Remote Sens. Environ*., *66*, 1–16, https://doi.org/10.1016/S0034-4257(98)00031-5

Hou, W., Wang, J., Xu, X., Reid, J., Janz, S. & Leitch, J. (2020). An algorithm for hyperspectral remote sensing of aerosols: 3. Application to the GEO-TASO data in KORUS-AQ field campaign. *Journal of Quantitative Spectroscopy & Radiative Transfer*., *253*, 22.

Kahn, R. A., & B. J. Gaitley (2015). An analysis of global aerosol type as retrieved by MISR. *Journal of Geophysical Research: Atmospheres*, *120*, 4248–4281, doi:10.1002/ 2015JD023322.

Kahn, R., West, R., McDonald, D., Rheingans, B., & Mishchenko, M. I. (1997). Sensitivity of multiangle remote sensing observations to aerosol sphericity. *Journal of Geophysical Research: Atmospheres*, *102*, NO. D14, 16,861–16,870.

Knapp, K. R., Frouin, R. Kondragunta, S., & Prados, A. (2005). Toward aerosol optical depth retrievals over land from GOES visible radiances: determining surface reflectance. *Int. J. Remote Sens.*, *26 (18)*, 4097–4116.

Letu, H., Nagao, T. M., Nakajima, T. Y., Riedi, J., ishimoto, H., Baran, A. J., et al. (2019). Ice cloud properties from Himawari-8/AHI next-generation geostationary satellite: Capability of the AHI to monitor the DC cloud generation process. *IEEE Transactions on Geoscience and Remote Sensing*, *57*, 3229–3239.

Levy, R. C., Remer, L. A., & Dubovik, O. (2007). Global aerosol optical properties and application to Moderate Resolution Imaging Spectroradiometer aerosol retrieval over land. *J. Geophys. Res*., *112(D13210)*, doi:0.1029/2006JD007811

Li, J., Carlson, B. E., & Lacis, A. A. (2015). Using single-scattering albedo spectral curvature to characterize East Asian aerosol mixtures. *J. Geop hys. Res. Atmos*.,120, 2037–2052, doi:10.1002/2014JD022433.

Limbacher, J. A. & Kahn, R. A. (2019). Updated MISR dark water research aerosol retrieval algorithm – Part 2: Aerosol and surface-reflectance retrievals over shallow, turbid, and eutrophic water. *Atmos. Meas. Tech*. *12*, 675–689, doi:10.5194/amt-12-675-2019.

Magzamen, S., Gan, R. W., Liu, J., O'Dell, K., Ford, B., Berg, K., et al. (2021). Differential cardiopulmonary health impacts of local and long-range transport of wildfire smoke. *GeoHealth*, *5*, e2020GH000330. https://doi.org/10.1029/2020GH000330

Mecikalski, J. R., Rosenfeld, D., & Manzato, A. (2016). Evaluation of geostationary satellite observations and the development of a 1–2 h prediction model for future storm intensity, *Journal of Geophysical Research: Atmospheres*, *121*, 6374–6392, doi:10.1002/2016JD024768

Meng, Z., Yang, P., Kattawar, G. W., Bi, L., Liou, K. N., & Laszlo, I. (2010): Single-scattering properties of nonspherical mineral dust aerosols: A database for application to radiative rransfer calculations, *J. of Aerosol Science*, *41*, 501-512.

Miller, S. D. (2003). A consolidated technique for enhancing desert dust storms with MODIS. *Geophys. Res. Lett*., *30(20*), 2071, doi:10.1029/2003GL018279

Muñoz, O., Volten, H., de Haan, J. F., Vassen, W., & Hovenier, J. W. (2001). Experimental determination of scattering matrices of randomly oriented fly ash and clay particles at 442 and 633 nm. *J. Geophys. Res.*, 106**,** 22833–22844. https://doi.org/10.1029/ 2000JD000164.

Nichols, N. T. A. (2020). Saharan Dust and Pediatric Asthma: A Multinational, Multiyear Assessment in the Caribbean, (Doctoral dissertation). Retrieved from Eugene McDermott Library (https://hdl.handle.net/10735.1/9137), Dallas, the University of Texas.

Omar, A. H., Winker, D. M., Tackett, J. L., Giles, D. M., Kar, J., Liu, Z., Vaughan, M. A., Powell, K. A., & Trepte, C. R. (2013). CALIOP and AERONET aerosol optical depth comparisons: One size fits none. *Journal of Geophysical Research: Atmospheres*, *118*, 4748–4766, doi:10.1002/jgrd.50330

Prospero, J. M., & Lamb, P. J. (2003). African droughts and dust rransport to the Caribbean: Climate change implications. *Science*, *302*, 1024–1027, https://doi.org/10.1126/science.1089915

Remer, L. A., Kaufman, Y. J., et al. (2005). The MODIS aerosol algorithm, products, and validation. *J. Atmos. Sci*., *62(4*), 947-973.

Remer, L. A., Tanré, D., Kaufman, Y. J., Levy, R. C., & Mattoo, S. (2006). Algorithm for remote sensing of tropospheric aerosol from MODIS: Collection 5, Product ID MOD04/MYD04.

Saito, M., Yang, P., Ding, J. & Liu, X. (2021). A comprehensive database of the optical properties of irregular aerosol particles for radiative transfer simulations. *J. Atmos. Sci*., https://doi.org/10.1175/JAS-D-20-0338.1

Schmit, T. J., Griffith, P., Gunshor, M. M., Daniels, J. M., Goodman, S. J., & Lebair, W. J. (2017). A Closer Look at the ABI on the GOES-R Series. *B. Am. Meteorol. Soc*., *98*, 681–698.

Shi, Y. R., Levy, R. C., Eck, T. F., Fisher, B., Mattoo, S., Remer, L. A., Slutsker, I., & Zhang, J. (2019). Characterizing the 2015 Indonesia fire event using modified MODIS aerosol retrievals. *Atmos. Chem. Phys*., *19*, 259–274, https://doi.org/10.5194/acp-19-259-2019

Si, Y., Lu, Q., Zhang, X., Hu, X., Wang, F., Li, L., & Gu, S. (2021). A review of advances in the retrieval of aerosol properties by remote sensing multi-angle technology. *Atmospheric Environment*, *244* (1): 117928.

Sorensen, C., House, J. A., O'Dell, K., Brey, S. J., Ford, B., Pierce, J. R., et al. (2021). Associations between wildfire-related PM2.5 and Intensive Care Unit Admissions in the United States, 2006–2015., *GeoHealth*, accepted.

Spurr, R., Kurosu, T., & Chance, K. (2001), A linearized discrete ordinate radiative transfer model for atmospheric remote-sensing retrieval. *J. Quant. Spectrosc. Radiat. Transfer*, *68*, 689–735.

Tanré, D., & Kaufman, Y. J., et al. (1997). Remote sensing of aerosol properties over oceans using the MODIS/EOS spectral radiances. *J. Geophys. Res*., *102*(D14), 16971–16988.

Vermote, E. F., Slonaker, R., Vibert, S., Petrenko (2006). National Polar-orbiting Operational Environmental Satellite System (NPOESS) VIIRS Aerosol optical thickness and particle size parameter algorithm theoretical basis document, Version 5, Revision 8: June 2006, Document #: Y2388

Volten, H., Muñoz, O., Rol, E., de Haan, J. F., Vassen, W., & Hovenier, J. W. (2001). Scattering matrices of mineral aerosol particles at 441.6 nm and 632.8 nm. *J. Geophys. Res*., *106*, 17375–17401. https://doi.org/10.1029/2001JD900068

Wang, Y., Chen, L., Xin, J., & Wang, X (2020). Impact of the dust aerosol model on the VIIRS aerosol optical depth (AOD) product across China. *Remote Sens*., *12*, 991. https://doi.org/10.3390/rs12060991

Wang, J., Liu, X., Christopher, S. A., Reid, J. S., Reid, E. A., & Maring, H. (2003a). The effects of non-sphericity on geostationary satellite retrievals of dust aerosols. *Geophys. Res. Lett*., 30, 2293, doi:10.1029/2003GL018697

Wang, J., Christopher, S. A., Reid, J. S., Maring, H., Savoie, D., Holben, B. H., Livingston, J. M., Russell, P. B., & Yang, S. K. (2003b). GOES-8 retrieval of dust aerosol optical thickness over the Atlantic Ocean during PRIDE, *J. Geophys. Res*., *108*, 8595, doi:10.1029/2002JD002494.

Wang, J., Xu, X., Ding, S., Zeng, J., Spurr, R., Liu, X., Chance, K., & Mishchenko, M. (2014). A numerical testbed for remote sensing of aerosols, and its demonstration for evaluating retrieval synergy from a geostationary satellite constellation of GEO-CAPE and GOES-R. *J. Quant. Spectrosc. Radiat. Transfer*., *146*, 510–528.

Westphal, D. L., et al. (2009). Operational aerosol and dust storm forecasting. *IOP Conf. Ser.: Earth Environ. Sci*., *7*, 012007, https://iopscience.iop.org/article/10.1088/1755-1307/7/1/012007

Witek, M. L., Garay, M. J., Diner, D. J., & Smirnov, A. (2019). Oceanic aerosol loading derived from MISR's 4.4 km (V23) Aerosol Product. *Journal of Geophysical Research: Atmospheres*, *124*, 10,154–10,174. https://doi.org/ 10.1029/2019JD031065

606 Xu, X. & Wang, J. (2015). Retrieval of aerosol microphysical properties from AERONET photo-
607 polarimetric measurements: 1. Information content analysis. *J. Geophys. Res.*, *120*, 7059–
608 7078, doi:10.1002/2015JD023108
609 Xu, X. & Wang, J. (2019). UNL-VRTM, a testbed for aerosol remote sensing: Model
610 developments and applications, in Springer Series in Light Scattering, Vol 4, edited by A.
611 Kokhanovsky, pp. 1-69, Springer, Cham, doi:10.1007/978-3-030-20587-4_1
612 Xu, X., Wang, J., Zeng, J., Spurr, R., Liu, X., Dubovik, O., Li, L., Li, Z., Mishchenko, M., Sinyuk,
613 A., & Holben, B. (2015). Retrieval of aerosol microphysical properties from AERONET
614 photo-polarimetric measurements: 2. A new research algorithm and case demonstration. *J.*
615 *Geophys. Res.*, *120*, 7079–7098, doi:10.1002/2015JD023113
616 Yang, Y., Zhao, C., Sun, L., & Wei, J. (2019). Improved aerosol retrievals over complex regions
617 using NPP Visible Infrared Imaging Radiometer Suite observations. *Earth and Space*
618 *Science*, 6, 629–645. https://doi.org/10.1029/2019EA000574
619 Zhang, H., Hoff, R. M., Kondragunta, S., Laszlo, I., & Lyapustin, A. (2013). Aerosol optical
620 depth (AOD) retrieval using simultaneous GOES-East and GOES-West reflected radiances
621 over the western United States. *Atmos. Meas. Tech.*, *6*, 471–486.
622 Zhang, H., Kondragunta, S., Laszlo, I., & Zhou, M (2020). Improving GOES Advanced Baseline
623 Imager (ABI) aerosol optical depth (AOD) retrievals using an empirical bias correction
624 algorithm. *Atmos. Meas. Tech*., *13*, 5955–5975, https://doi.org/10.5194/amt-13-5955-2020
625 Zhou, Y., Levy, R. C., Remer, L. A., Mattoo, S., Shi, Y., & Wang, C. (2020). Dust aerosol
626 retrieval over the oceans with the MODIS/VIIRS Dark-Target algorithm: 1. Dust detection.
627 *Earth and Space Science*, *7*, e2020EA001221. https://doi.org/10.1029/2020EA001221